

Supplementary Material:

Polarization-dependence of palladium deposition on ferroelectric lithium niobate (0001) surfaces

Seungchul Kim, Michael Rutenberg Schoenberg, and Andrew M. Rappe*

*The Makineni Theoretical Laboratories, Department of Chemistry,
University of Pennsylvania, Philadelphia, Pennsylvania 19104-6323, USA*

(Dated: June 20, 2011)

ATOMIC MODEL OF LITHIUM NIOBATE SUBSTRATES

The ferroelectric phase of lithium niobate (LiNbO_3 , LNO) has a bulk structure consisting of layers in a Li-O₃-Nb pattern [2]. Here we show LiNbO_3 with its thermodynamically preferred surface terminations, as predicted by Levchenko and Rappe (Fig. S1). Li atoms are added to the positive (c^+) surface, and both Li and O atoms are added to the negative surface (c^-) of LiNbO_3 for charge passivation. Passivation atoms are denoted Li' and O' . These surface terminations make the overall stoichiometry of five trilayer slab used in this study, from c^+ (left) to c^- (right), $\text{Li}'\text{-(Li-O}_3\text{-Nb)}_5\text{-Li}'\text{O}'$.

SUPPLEMENTARY DFT METHODS

In all density functional theory (DFT) total energy calculations [3], we used $3 \times 3 \times 1$ k -point grids [4], plane wave energy cutoffs of 50 Ry. When necessary, we included spin as a degree of freedom in our calculations. We checked the convergence of our monomer and dimer adsorption energies calculated in $\sqrt{3} \times \sqrt{3}$ supercells on five layer thick slabs by using either $\sqrt{7} \times \sqrt{7}$ supercells or seven trilayer thick slabs. The resulting energies agreed within 0.1 eV/Pd. During the geometric optimization, we allowed relaxation of Pd atoms and the first two layers

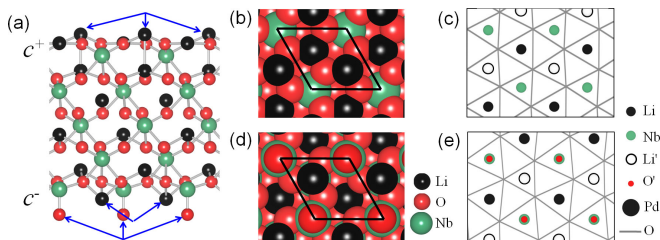


FIG. S1: Geometry of five-trilayer LiNbO_3 slab: (a) side view, (b,c) top view of c^+ , and (d,e) top view of c^- . Slabs are represented using ball and stick (a) and space filling (b,d) models, or the simplified model used in the main text (c,e). Blue arrows in (a) denote ions (Li' and O') introduced for surface charge passivation. Black lines in (b) and (d) indicate the boundaries of the LiNbO_3 primitive surface unit cell. (b) and (d) are redrawn from Ref. [1].

# of Pd atoms	positive (c^+)		negative (c^-)			free Pd _n
	E_{ads}^m	E_{ads}^c	E_{ads}^m	E_{ads}^c	$E_{\text{bond}}^{\text{Pd-X}}$	$E_{\text{bond}}^{\text{Pd-Pd}}$
1	0.95	0.95	2.02	2.02	1.01	–
2	1.45	0.62	2.00	1.44	1.01	1.15
3	2.28	0.44	2.79	1.15	1.13	1.12
4	2.68	0.26	2.55	0.77	1.02	1.05
5	–	–	2.39	0.65	0.98	0.94

cohesive energy of Pd bulk (GGA-PBE) = 3.57 eV

TABLE S1: Marginal adsorption energies of the last adatom (E_{ads}^m), and per-atom adsorption energies of Pd clusters on LNO surfaces relative to infinitely separated free Pd clusters and LNO slabs (E_{ads}^c). We define $E_{\text{ads}}^m = E_{\text{Pd}_{n-1}\text{LNO}} + E_{\text{Pd}} - E_{\text{Pd}_n\text{LNO}}$ and $E_{\text{ads}}^c = (E_{\text{LNO}} + E_{\text{Pd}_n} - E_{\text{Pd}_n\text{LNO}})/n$, where n is the number of Pd atoms. $E_{\text{Pd}_n\text{LNO}}$, E_{Pd} , E_{Pd_n} and E_{LNO} are DFT total energies of the Pd cluster (Pd_n) adsorbed on LNO, free Pd atom, free Pd cluster and LNO slab, respectively. On the c^- surface, we report average Pd-X bond energies, $E_{\text{bond}}^{\text{Pd-X}} = (E_{\text{LNO}} + nE_{\text{Pd}} - E_{\text{Pd}_n\text{LNO}})/N_{\text{bond}}^{\text{Pd-X}}$, where $N_{\text{bond}}^{\text{Pd-X}}$ is the number of Pd-X bonds. We also report average Pd-Pd bond energies, $E_{\text{bond}}^{\text{Pd-Pd}}$, of free Pd clusters and a cohesive energy of bulk Pd for comparison. All energies are given in eV.

of the LiNbO_3 surface, but kept the remaining portion of the slab fixed, and used a force tolerances of 0.01 eV/Å. To remove spurious interactions between different supercells, we separated the slabs with more than 13 Å of vacuum and employed a dipole correction [5].

ADSORPTION ENERGIES

In our analysis of the energetics of Pd adsorption on LiNbO_3 , we consider two quantities for adsorption energy, E_{ads}^m and E_{ads}^c , defined as the marginal adsorption energy of the last adatom (E_{ads}^m) and per-atom adsorption energy of a cluster relative to the free clusters and the LNO slabs (E_{ads}^c), as listed in Table S1. Structures of adsorbed cluster are drawn in Fig. 1 in the main text; their shapes are qualitatively same as free clusters with slight deformations, with one exception, the pentamer on c^- . Free clusters are in the shapes of triangle, tetrahedron and square pyramid for Pd_3 – Pd_5 [6]. However, the last adatom of Pd_5 on c^- bonds to the edge of the tetrahedral Pd_4 , such that that adatom bonds only with two

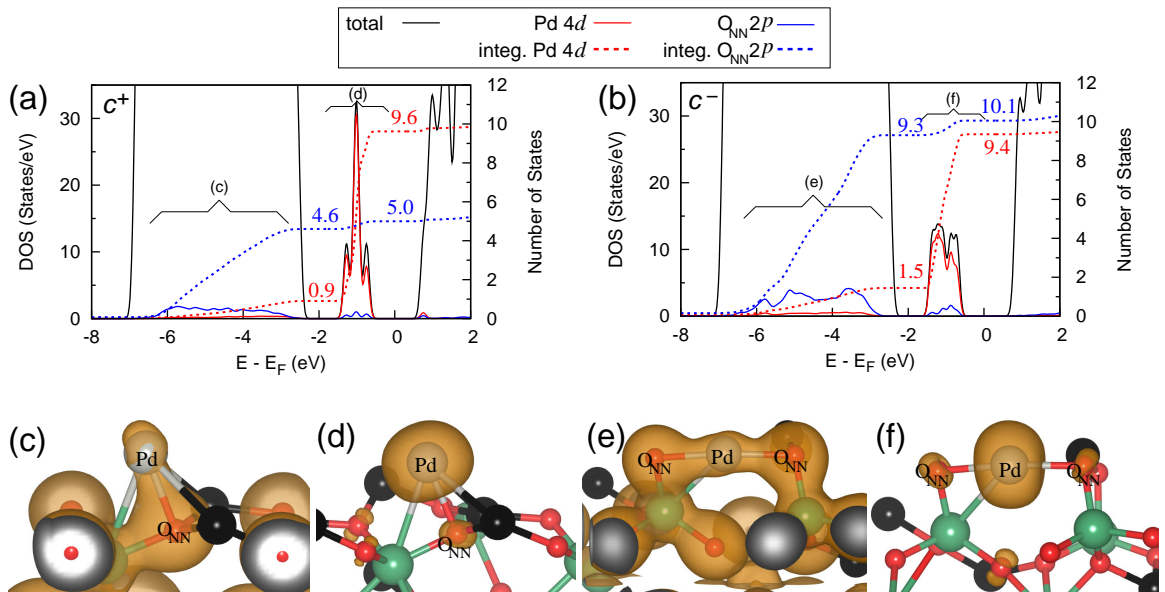


FIG. S2: (a) and (b) are projected density of states (PDOS, solid lines) and integrated PDOS (dotted lines) of monoatomic Pd adsorption for the c^+ and c^- surfaces, respectively. (c)–(f) are integrated local density of states (ILDOS) for energy ranges noticed in (a) and (b). ILDOS is defined as the sum of wave function squares whose eigenvalue lies in given energy range, $\sum_{E_1 < \epsilon_i < E_2} |\psi_i(\vec{r})|^2$ for the energy range (E_1, E_2) , where ϵ_i is the eigenenergy of Kohn-Sham state ψ_i . Same isosurface values were used at (c)–(f). O_{NN} is the nearest neighbor oxygen of Pd.

Pd atoms (See Fig. 1 (d) in the main text).

We note that on the c^+ surface, E_{ads}^c becomes smaller as the number of Pd atoms increases. This lowering of the bonding energy is due to mismatch between ideal the Pd-Pd bond lengths and the distances between Pd binding sites. In contrast, E_{ads}^c remains relatively high even for pentamers on the c^- surface, largely due to many Pd-O' bonds. In the main text, we explained many of our conclusions about energetics on the c^- surface in terms of the total number of Pd-Pd and Pd-O' bonds (hereafter denoted Pd-X bonds). This analysis was justified by the fact that average Pd-X bond energies ($E_{\text{bond}}^{\text{Pd-X}}$), defined as free-atom-relative adsorption energy divided by the number of Pd-X bonds (N_{bond}), were similar for all cluster sizes studied and were also similar to average bond energies in free Pd clusters (E_{bond}^c). We show explicit values for $E_{\text{bond}}^{\text{Pd-Pd}}$ and $E_{\text{bond}}^{\text{Pd-X}}$ in Table S1. Overall, Pd atoms are adsorbed more strongly on the c^- surface than on the c^+ surface. However, agglomeration is favored on both surfaces; E_{ads}^m of clusters are larger than that of monomer. E_{ads}^m of dimer on c^- is smaller than that of monomer, indicating the dimer is the critical nuclear, but this fact does not change agglomeration behavior qualitatively. Thus, no qualitative difference between two surfaces is expected from the thermodynamic point of view.

Since Pd-O' bonding makes the key contribution to the difference in adsorption behavior between the c^+ and c^- surfaces, we wanted to be sure that DFT-GGA does not misestimate the favorability of Pd-O interactions. To do

this, we considered the case of bulk PdO. We compared our DFT-GGA energy of formation of PdO from individual Pd and O atoms, defined as $E_{\text{Pd}}^{\text{atom}} + E_{\text{O}}^{\text{atom}} - E_{\text{PdO}}^{\text{bulk}}$, to the sum of the experimental values for PdO formation energy [7], Pd bulk cohesive energy [8], and half of the O_2 bonding energy [9]. Our DFT-calculated value was only 2.1% greater than the experimental value, suggesting that DFT predicts Pd-O interactions well and that the strong Pd-O interactions seen on the c^- surface are valid. As a note, we did not use the DFT PdO formation energy as a metric for comparison, because DFT-GGA is known to predict the energy of O_2 quite poorly [9].

ELECTRONIC STRUCTURES OF MONOMER ADSORPTION

Our KMC simulations show significant differences between Pd clustering on the c^+ and c^- surfaces of LiNbO_3 . Thus far, we have explained these differences in terms of the different geometries of the c^+ and c^- surfaces themselves, which result from the presence of different atoms on each of the surfaces for surface charge passivation. However, since the surfaces have opposite polarizations, it is also necessary to investigate whether there are electronic differences in the bonds formed or Pd itself that Pd upon adsorption onto the two surfaces.

We present projected density of states (PDOS) and integrated local density of states (ILDOS) of both the c^+ and c^- surfaces ,after adsorption of a single Pd atom, in

Fig. S2. To achieve converged DOS We used denser k -point grids, $9 \times 9 \times 1$ in $\sqrt{3} \times \sqrt{3}$ surface unit cells, than in atomic structure relaxations. (c)–(f) show the integrated local density of states (ILDOS) for energy ranges denoted in (a) and (b). PDOS are calculated using Löwdin charge analysis [10, 11], and ILDOS is defined as the sum of the square of wave functions whose eigenvalues lie in given energy range, that is, ILDOS is $\sum_{E_1 < \varepsilon_i < E_2} |\psi_i(\vec{r})|^2$ for the energy range (E_1, E_2) . Here, ε_i is the eigenenergy of Kohn-Sham state ψ_i . Note that there are two O_{NN} for c^- so that DOS of O_{NN} for c^- is much larger than that for c^+ .

Our results show that on both surfaces, Pd makes bonds to O_{NN} with primarily covalent character. The PDOS contributions of Pd and O_{NN} on both surfaces occur over two distinct energy ranges (-6.5,-2.5 eV; -0.5, 1.5 eV). In the lower range, we see significant overlap between Pd $4d$ and O_{NN} $2p$ orbitals. Pd $4d$ contributes $0.9 e^-$ to this energy range on the c^+ surface, and $1.5 e^-$ on c^- . This is consistent with the fact that Pd has two neighboring oxygen atoms on the c^- surface, while only one on c^+ . The ILDOS for this energy range shows explicitly that there is large electron density between the Pd and O_{NN} atoms on both surfaces, indicating that covalent bonds are being formed. In the higher energy range, PDOS of Pd $4d$ on the c^+ surface is sharper and a little narrower than that on the c^- surface. However, overall behavior on the c^+ and c^- surfaces is also similar. In this range, contributions from the Pd $4d$ orbitals dominate, while O_{NN} $2p$ orbitals make a small contribution. In contrast to the lower energy range, hybridization of Pd and O_{NN} orbitals are very small. A covalent character of Pd- O_{NN} is further confirmed by the fact that net charges on Pd are very small on both surfaces ($+0.4 |e|$ on c^+ , $+0.6 |e|$ on c^-), implying small ionic bonding character.

Electronic structures strongly imply that there is little difference in bonding type of Pd on two surfaces, and different adsorption energies and transition barriers originate from geometric difference (e.g. the number of the neighboring oxygens) which is the consequence of surface stoichiometry. One could expect that charges of poled LiNbO_3 surfaces affect Pd adsorption energy and its electronic structures. However, most of surface charges are compensated already by ions [1] so that the effect of surface charge on electronic structures of Pd will be small. Polarization effect on Pd adsorbate is indirect via atomic structure of surfaces (i.e. polarization-induced inequivalent surface termination) rather than direct such as surface charge.

KINETIC MONTE CARLO SIMULATION DETAILS

Our kinetic Monte Carlo (KMC) simulations were performed in periodic $10 \text{ nm} \times 10 \text{ nm}$ cells. We included 15

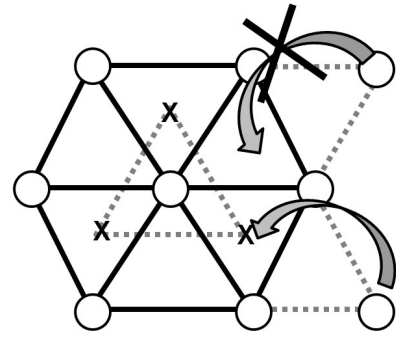


FIG. S3: An FCC lattice is not sufficient to allow all possible agglomeration events to occur. Of the two agglomeration processes pictured, one is allowed by the FCC lattice, while the other, denoted by a ‘X’, would also require HCP lattice points on the second layer of the simulation lattice. We thus used an A-(ABC)-(ABC)⋯ lattice as described in the text. Open circles denote Pd atoms and ‘X’s denote points on the second layer of the simulation lattice.

layers of Pd binding sites above the surface, though no Pd atoms reached the top layer of the cell in any of our simulations. All Pd binding sites on the layer in contact with the LiNbO_3 surface were mapped onto their corresponding points on the triangular oxygen lattice. Beginning with the second layer above the surface, we used three sublattices to allow all possible Pd cluster configurations such that the lattice is substrate-A-(ABC)-(ABC)⋯. The use of this lattice, which is much denser than the face-centered cubic (FCC) lattice of bulk Pd, was necessary to describe some diffusion events that can occur for small numbers of Pd atoms, but is forbidden by the FCC lattice. For example, half of all possible agglomeration processes are forbidden using an FCC lattice, because lattice points are present that correspond to only half of the surface’s hollow sites (Fig. S3). Additionally, hopping of Pd atoms between FCC and hexagonal close-packed (HCP) hollow sites on (111) cluster facets is forbidden by a pure FCC lattice. To compensate for the fact that some points in the lattice used in our simulation are closer together than a reasonable Pd-Pd bond distance, we imposed two rules. First, the same site cannot be occupied on adjacent layers of the lattice. Additionally, within the same layer, adjacent sites on different sublattices cannot be occupied.

We built our simulations primarily based on our DFT calculations of the activation barriers of diffusion and agglomeration of up to four atoms. On the c^+ surface, it was unnecessary to consider diffusion of larger clusters, because our deposition time interval was sufficiently long that we observed monomers to aggregate into clusters before other monomers are deposited in the same vicinity. Diffusion of large clusters on the c^- surface could also be neglected, because they require the breaking of two or more Pd-X bonds and thus have activation barriers

sufficient to prevent their occurrence on the time scale that we considered. As described below, in cases where we had not calculated activation barriers directly, such as monoatomic motion on cluster facets, we interpolated reasonable barriers.

We permitted diffusion of Pd atoms that were directly in contact with the LiNbO_3 surface or on cluster facets. On the LiNbO_3 surface, we permitted the following diffusion processes: 1) nearest-neighbor monomer hopping, 2) agglomeration/deagglomeration (movement of Pd atom from layer 1 (2) onto layer 2 (1)), 3) dimer walking and sliding on c^+ , 4) trimer walking and sliding on c^+ , 5) trimer flipping on c^- , 6) tetramer rolling and 7) dissociation (some of these processes are pictured in Fig. 2 in the main text). On cluster facets, we permitted monomer hopping only. Though concerted movements of multiple atoms can occur on metal cluster facets, these generally affect cluster morphology, but not cluster size (number of atoms present). Since our primary interest is only in seeing differences in cluster size, this simplification of Pd behavior on cluster facets is acceptable.

It is well known that the activation barriers for monomeric diffusion on the (111) surfaces of FCC metals are quite low relative to the bulk metal-metal bond energy. Our nudged elastic band (NEB) calculations show that the activation barrier for monoatomic hopping from from FCC to HCP hollow sites on (111) surface of palladium is 0.11 eV, despite the fact that the Pd-Pd bulk bond energy is nearly six times larger (0.59 eV). This is explained by the fact that during monomer hopping between nearest-neighbor sites, new bonds start to form before others are completely broken. In our KMC simulations, we interpolated reasonable activation barriers for diffusion events on Pd cluster facets using insights from Trunshin and coworker's studies of nearest-neighbor monoatomic hopping on copper surfaces and steps [12]. By compensating for the difference in cohesive energy between bulk Pd and Cu, we estimated that the activation barrier for nearest neighbor monomer hopping is 0.2 eV per Pd-Pd bond broken during transition state formation. We also showed that the qualitative results of some of our simulations were insensitive to the use of a 0.3 eV barrier for this process. In next nearest neighbor monomer hopping, which is analogous to the agglomeration processes pictured in Fig. 2 but generalized to movements between any two levels in the simulation lattice (starting with level 2), Pd-Pd bonds are broken completely during transition state formation. Thus, we estimated the activation barrier for this process based on the cost of Pd-Pd bond breaking. The cost of breaking a bond in a Pd_{20} cluster cut from bulk Pd is 0.52 eV. Similarly the cost of dimer dissociation is 0.55 eV. Thus, for next-nearest neighbor hopping on Pd cluster facets, we used a barrier of 0.5 eV per Pd-Pd bond broken.

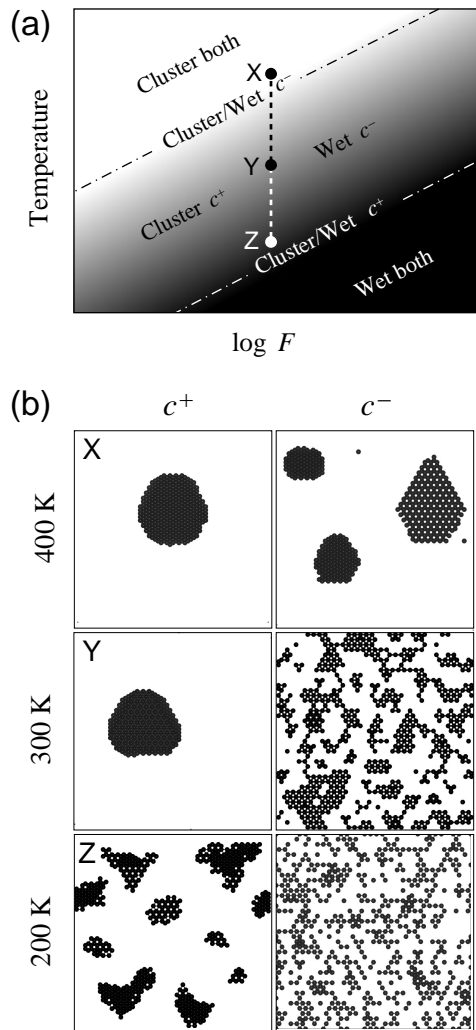


FIG. S4: (a) graphical representation of temperature and deposition rate (F) dependence of wettability. The logarithmic behavior of F is due to the exponential dependence of hopping time on temperature. (b) snapshots of KMC simulations at 0.5 ML coverage. Deposition rate is 0.025 ML/s for all cases. 'X', 'Y' and 'Z' denote the points in (a).

TEMPERATURE AND DEPOSITION RATE DEPENDENCE OF WETTABILITY

Despite the various kinetic parameters involve to the deposition process, cluster sizes are dominantly determined by two characteristic time scales: the time for a new atom to arrive to the surfaces (set by deposition rate) and the time of an atom to hop (set by energy barrier and temperature). We show how wettability depends on temperature and deposition rate (F) in Fig. S4. A fast deposition corresponds to short time for additional atoms to come, and low temperature corresponds to long time for atoms to hop. Thus, these conditions lead to dispersed deposition geometry. The reverse is true for slow deposition and high temperature conditions.

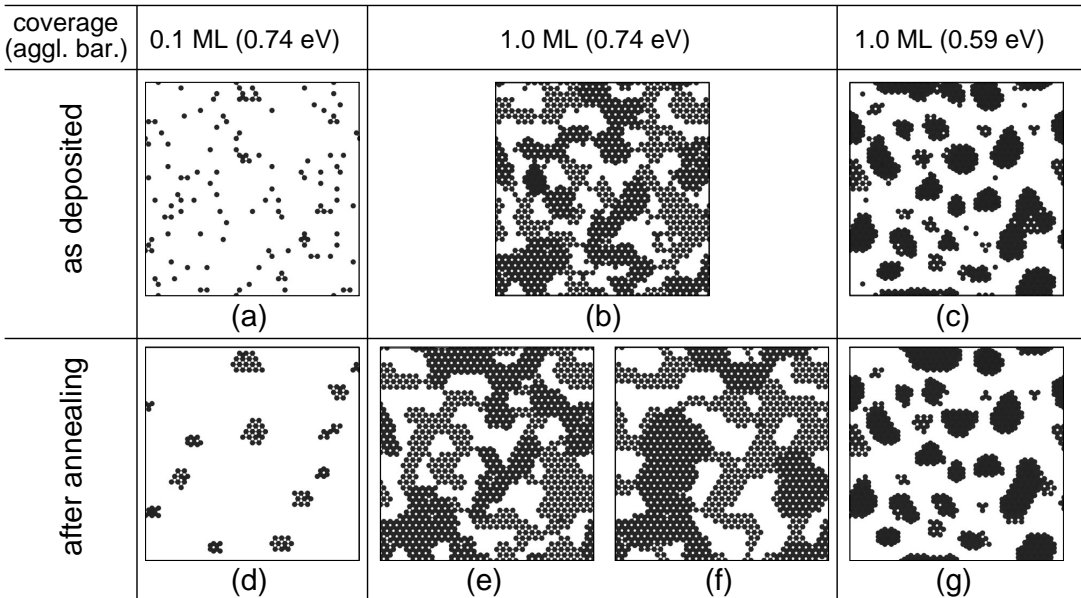


FIG. S5: Pd adsorption geometries predicted by kinetic Monte Carlo simulations on the c^- surface of LiNbO_3 immediately after deposition ends (a-c) and 2-15 minutes later (d-e). These simulations were conducted at different coverages (0.1 ML and 1.0 ML), different temperatures (300 and 400 K), and with the two different agglomeration barriers predicted by DFT (0.59 eV and 0.74 eV). All simulations were conducted at a deposition rate of 0.025 ML/s. Times waited after the completion of deposition were: (d) 15 minutes, (e) 10 minutes, (f) 2 minutes, and (g) 3 minutes. All simulations are conducted at 300 K, except for (f), which is at 400 K.

Because cluster diffusion barriers of c^+ ($\lesssim 0.4$ eV) and c^- ($\gtrsim 0.8$ eV) are much different, there is a range of temperature and deposition rate at which palladium wets c^- while that is clustered on c^+ . As discussed in the main text, the room temperature and experimentally convenient deposition rates (e.g. 0.01–0.1 ML/s) correspond to this range. Fig. S4 (b) shows snapshots of KMC simulations of 0.5 ML coverage at three temperatures when the deposition rate is 0.025 ML/s. As opposed to 300 K where only one cluster takes shape, several clusters do once the temperature drops to 200 K (Fig. S4 (b)). Since the monomer diffusion barrier on c^- is approximately twice that of the barrier on c^+ , several clusters were observed at 400 K on c^- . The difference in number of clusters (three vs. nine) are due to other kinetic parameters and different critical nuclear sizes (1 for c^+ and 2 for c^-) [13]. At these few-cluster forming temperatures, 200 K for c^+ and 400 K for c^- , we have observed that the cluster sizes are dependent on deposition rate, as what we have found when we changed the rate from 0.01 ML/s to 0.1 ML/s.

AGGREGATION AND AGGLOMERATION ON c^- AFTER DEPOSITION

The relatively large diffusion barriers on the c^- surface (≈ 0.8 eV) were not sufficiently high to prevent agglomeration completely, especially when our simulations were

extended until slightly after deposition was complete. We have conducted KMC simulations during deposition and after annealing for 2-15 minutes for both low (0.1 ML) and high (1.0 ML) coverages and at different temperatures (300 or 400 K). We also conducted our simulations with agglomeration barriers (0.59 and 0.74 eV) for the two different possible cluster agglomeration processes predicted by DFT on the c^- surface (See Fig. 2(g,h) and Table I in the main text). These data are reported in Fig. S5.

At low coverage (0.1 ML), Pd atoms are highly dispersed at the end of deposition (Fig. S5(a)). However, within 15 minutes, all but two Pd clusters are immobile, suggesting that on a slightly longer time scale, all Pd atoms will join immobile clusters (Fig. S5(d)). However, these clusters are quite small compared to the single cluster that forms on the c^+ surface under the same conditions. Two factors contribute to the formation of smaller clusters on the c^- surface than on c^+ : lower maximum mobile cluster size, and the higher number density of clusters on the surface during deposition. On the c^+ surface, the mismatch between the distances between monomeric Pd binding sites and Pd-Pd equilibrium bond distances makes the activation barrier for motion of relatively large clusters rather low. For example, our predicted barrier for tetramer rolling was similar to that for monomer hopping, largely because this process requires movement of only one Pd atom out of a monomeric potential well. Other work suggests that this condition may

be met by Pd clusters as large as 13 atoms [14], and thus, that clusters of this size may be mobile on the c^+ surface. In contrast, the diffusion of clusters larger than a tetramer on the c^- surface requires breakage of at least two Pd-X bonds, making these diffusion events extremely unlikely on the time scale of deposition. A second factor contributing to the formation of large clusters on the c^+ surface is the fact that, because barriers for diffusion are so low, many diffusion events can occur during the average waiting time between addition of new atoms to the simulation cell on this surface. This means that only a few atoms at a time will be separate from the large immobile cluster, greatly reducing the probability that a second immobile cluster will form. The opposite is true on the c^- surface, where larger diffusion barriers mean that on average multiple Pd atoms are deposited inside the simulation cell between diffusion events of a single atom or cluster. As a result, many individual clusters are present in any given area of the simulation cell, promoting the formation of many small immobile clusters.

At high coverage (1.0 ML), Pd atoms continue to rearrange after deposition is complete until all atoms make at least three Pd-X bonds (Fig. S5(b,e)). Once this occurs, agglomeration can only occur on an extremely long time scale, because it requires breakage of multiple Pd-X bonds. Thus, the Pd coverage area of these clusters will remain relatively constant. This was true even when our surface was annealed at a higher temperature (400 K, Fig. S5(f)), consistent with the finding of Zhao and colleagues that the Pd geometry on the c^- surface is stable up to 425 K [15].

Even when we used the lower of our two agglomeration barriers predicted from DFT on the c^- surface (Fig. 2(g) in the main text), multiple distinct clusters formed at 1 ML coverage (Fig. S5(c,g)). At low coverage we observed results similar to those for the higher agglomeration barrier (Fig. S5(d)), but with taller individual clusters. Overall, our simulations with this lower agglomeration barrier on the c^- surface predicted Pd coverage

areas that were substantially higher than those on the c^+ surface, but lower than the simulations on the c^- surface with the higher agglomeration barrier.

In sum, our DFT and KMC calculations predict that though Pd forms slightly three dimensional clusters on the c^- surface of LiNbO₃, its overall adsorption pattern on this surface is much more dispersed than that on the c^+ surface.

* corresponding author: rappe@sas.upenn.edu

- [1] S. V. Levchenko and A. M. Rappe, Phys. Rev. Lett. **100**, 256101 (2008).
- [2] A. Saito, H. Matsumoto, S. Ohnisi, M. Akai-Kasaya, Y. Kuwahara, and M. Aono, Jap. J. Appl. Phys **43**, 2057 (2004).
- [3] J. Ihm, A. Zunger, and M. L. Cohen, J. Phys. C **12**, 4409 (1979).
- [4] H. J. Monkhorst and J. D. Pack, Phys. Rev. B **13**, 5188 (1976).
- [5] L. Bengtsson, Phys. Rev. B **59**, 12301 (1999).
- [6] C. Luo, C. Zhou, J. Wu, T. J. Dhillip Kumar, N. Balakrishnan, R. C. Forrey, and H. Cheng, International Journal of Quantum Chemistry **107**, 1632 (2007).
- [7] J. Nell and H. S. O'Neill, Geochimica et Cosmochimica Acta **60**, 2487 (1996).
- [8] C. Kittel, *Introduction to Solid State Physics* (John Wiley & Sons, Inc., 1996), seventh ed.
- [9] F. Furche, Phys. Rev. B **64**, 195120 (2001).
- [10] P.-O. Löwdin, J. Chem. Phys. **18**, 365 (1950).
- [11] D. Sanchez-Portal, E. Artacho, and J. M. Soler, Solid State Communications **95**, 685 (1995).
- [12] O. Trushin, A. Karim, A. Kara, and T. S. Rahman, Phys. Rev. B **72**, 115401 (2005).
- [13] H. Brune, Surface Science Reports **31**, 121 (1998).
- [14] W. Fan and X. Gong, Applied Surface Science **219**, 117 (2003).
- [15] M. S. H. Zhao, D. A. Bonnell, and J. M. Vohs, J. Vac. Sci. Technol. **27**, 1337 (2009).